Journal of Physics and Chemistry of Solids 172 (2023) 111050

Contents lists available at ScienceDirect

Journal of Physics and Chemistry of Solids

journal homepage: www.elsevier.com/locate/jpcs

FLA

Study of CaTiO3–ZnS heterostructure obtained by microwave-assisted solvothermal synthesis and its application in photocatalysis

Cátia L. Ücker [a,*], Suelen R. Almeida [a], Renato G. Cantoneiro [a], Lisiane O. Diehl [a], Sergio Cava [a], Mário L. Moreira [a], Elson Longo [b], Cristiane W. Raubach [a,**]

[a] CCAF – Advanced Crystal Growth and Photonics, CDTEC – Technological Development Center, Federal University of Pelotas, UFPEL, Pelotas, RS, 96010-610, Brazil
[b] CDMF-LIEC, UFSCar, P.O. Box 676, São Carlos, SP, 13565-905, Brazil

ARTICLE INFO

Keywords:
Heterostructure
Microwave-assisted solvothermal process
CTO
ZnS
Photocatalysis

ABSTRACT

We report herein the assembly of a calcium titanate (CTO)-zinc sulfide (ZnS) heterostructure through a microwave-assisted solvothermal (MAS) method and its respective characterizations to evaluate its material properties and applicability in heterogeneous photocatalysis. The CTO-ZnS heterostructure comprises a mixture of the orthorhombic crystalline phase of CTO and the cubic crystalline phase of ZnS. Scanning electron microscopy (SEM) images have revealed that the CTO consists of mesocrystals assembled from agglomerated microcubes. After applying a ZnS coating, it was possible to identify the formation of a cloud of particles around parts of the CTO mesocrystals, thus forming the heterostructure. The presence of ZnS on the CTO surface allowed for greater emission of photoluminescence, resulting in improved efficiency for photocatalytic applications. Photodegradation tests on Rhodamine B (RhB) dye in the presence of CTO, ZnS, and CTO-ZnS revealed that the heterostructure led to more extensive photocatalytic degradation (50.5%) within 30 min than CTO (10%). Moreover, the degradation efficiency over the CTO-ZnS increased to 95.7% after 180 min, indicating that the ZnS coating served to increase the degree of discoloration over time. These satisfactory results demonstrate that CTO-ZnS is a promising photocatalyst capable of accelerating the degradation of organic dyes, thus contributing to the decontamination of water resources. Scavenger tests revealed holes (h^+) to be the main active species in the photocatalytic process with CTO, whereas electrons (e^-), h^+, and hydroxyl radicals (HO^*) are all involved in the mechanism with both CTO-ZnS and ZnS.

1. Introduction

Environmental sustainability and the development of alternative and renewable energy supplies represent two of the major challenges of contemporary society [1,2]. As an excellent approach for the degradation of organic pollutants in water, heterogeneous photocatalysis can be applied to industrial wastewater for dispersing oil and removing surfactants and dyes [2–5]. Photocatalysis involves the activation of a photocatalyst, usually a semiconductor, through sunlight or artificial light with photonic energy equal to or greater than its band-gap energy [6,7]. In this process, an electron is excited from the valence band (VB) to the conduction band (CB), giving rise to pairs of photogenerated charges that may participate in reactions to produce highly oxidizing radicals to expedite the process of heterogeneous photocatalysis [8].

Perovskite-based oxide materials have interesting optical and electrical properties and are considered as potential catalysts to remove pollutants from the environment, in addition to their numerous other applications [9–12]. Calcium titanate ($CaTiO_3$), barium titanate ($BaTiO_3$), magnesium titanate ($MgTiO_3$), cobalt titanate ($CoTiO_3$), and strontium titanate ($SrTiO_3$) are perovskites that can be applied as ferroelectric materials, semiconductors, photorefractive materials, and catalysts due to their electrical, electro-optical, and electromechanical properties [13–17]. $CaTiO_3$ (CTO) is a perovskite-type ceramic semiconductor with an orthorhombic phase, a stable structure, and interesting optical, electrical, and magnetic properties [18,19]. Its main characteristic is its wide band gap of 3.5 eV [20,21]. Additionally, CTO is characterized by electron mobility, chemical stability, usability, ease of fabrication, and low cost [12,22–24]. For this reason, it is considered a good candidate as a photocatalyst for the removal of organic pollutants in photocatalytic processes [11,12,21,25]. However, it has a high

* Corresponding author.
** Corresponding author.
E-mail addresses: catiaucker@gmail.com (C.L. Ücker), craubach.iqg@ufpel.edu.br (C.W. Raubach).

https://doi.org/10.1016/j.jpcs.2022.111050
Received 20 April 2022; Received in revised form 13 October 2022; Accepted 16 October 2022
Available online 28 October 2022

recombination rate of electron/hole pairs, which limits its photocatalytic response [26].

One plausible method to improve the surface properties of materials is to assemble core–shell systems and heterostructures, which are obtained by placing two or more materials in proximity [27,28]. Heterostructures have a high charge-separation efficiency, which can increase the separation process and lifetime of photogenerated charges, allowing their application in photocatalytic processes with superior performance with respect to the individual components [1,29,30].

The coating material must have high selectivity and reactivity [27]. Various metal sulfides, such as CdS, ZnS, and CuS, have been used as photocatalysts [31]. Among them, ZnS is a II–VI semiconductor with fast generation of electron–hole pairs, which leads to greater photocatalytic activity [32]. ZnS is a non-toxic inorganic semiconductor with two characteristic crystal structures: cubic and hexagonal [33,34]. It has a wide band gap, ranging from 3.6 to 3.7 eV for cubic structures to approximately 4.0 eV for a hexagonal structure [35,36]. Moreover, ZnS has a high negative CB level, a high theoretical efficiency of photocarrier generation [37], good stability against oxidation and hydrolysis, and a high negative reduction potential to excite electrons [38,39]. Due to these structural and optoelectronic properties, ZnS has become an interesting material to be combined with CTO to form a heterostructure [40]. It is worth mentioning that ZnS has been widely used as a shell material, as in ZnO/ZnS [37,41], CdS@ZnS [31,42], CdSe@ZnS [43], $CsPbBr_3$/ZnS [44], and $AgInS_2$/ZnS [45], among others.

In some studies, photocatalytic degradation of dyes over heterostructures has been compared with that over the core material alone. Troque et al. [46] synthesized heterostructures based on titanate-ferrites ($SrTiO_3$–$CoFe_2O_4$ and $SrTiO_3$–$NiFe_2O_4$) by the hydrothermal method and found that both showed increased photocatalytic performance for RhB degradation (82% and 64%, respectively, after 240 min), compared to only 31% over pure $SrTiO_3$. Yan et al. [47] obtained Ag_2S@$CaTiO_3$ heterostructures by a conventional hydrothermal method and evaluated their photocatalytic performance for the degradation of RhB under UV irradiation, which was found to be about three times greater than that of pure $CaTiO_3$. Coleto Junior et al. [48] manufactured CaO/$SrTiO_3$ heterostructures and tested their photocatalytic activity for the degradation of RhB. According to the authors, the heterostructure achieved a discoloration efficiency of 92.5%, whereas the pure $SrTiO_3$ degraded only 37.4% in 120 min.

The characteristics of the synthesized material are defined by the methodology used, and various methods can be used to obtain heterostructures [49,50]. To compose heterostructures of CTO and ZnS, microwave-assisted solvothermal (MAS) synthesis was considered of interest due to its simplicity and processing advantages, such as homogeneous heating, clean reactions, high yields, and reduced synthesis times, in addition to fast crystallization and a simple nanopowder preparation process [51–53]. Besides, microwave-assisted synthesis is a highly recommended technique because microwaves interact directly with ions or molecules in solution and/or with solid phases dispersed in a liquid medium. It should be noted that the efficiency of converting microwave energy into thermal energy can be assessed by the physical variables of loss tangent, relaxation time, and depth of penetration [54–59]. As the effectiveness of the method depends on structural parameters, it is necessary to control the size uniformity, growth direction, and distribution of dopants within the nanostructure [60–62].

We are not aware of any previous studies on the fabrication of CTO-ZnS heterostructures by a microwave-assisted method. Therefore, in this work, we obtained a CTO-ZnS heterostructure by an MAS method, assessed the influence of ZnS on the surface of $CaTiO_3$, and analyzed the possible differences in the properties of the heterostructure compared to pure CTO through various characterization techniques. In addition, the photocatalytic performance of the heterostructure for the degradation of RhB under UVC light illumination was also evaluated in comparison with that of pure uncoated CTO. Inspection by microscopy analyses showed the formation of a cloud of ZnS particles around the CTO. The presence of ZnS on the surface of the CTO led to a better photocatalytic performance than that of pure CTO due to greater absorption of light on the surface of the heterostructure, which facilitated charge transfer. Lastly, the kinetics of photogenerated reactive species and reuse of the photocatalyst were also investigated. The catalyst described herein has proved to be advantageous, with good prospects for application in the degradation of organic pollutants.

2. Materials and methods

2.1. CTO synthesis

CTO was obtained through MAS synthesis. To this end, two solutions were prepared. First, titanium isopropoxide ($C_{12}H_{28}O_4Ti$, Sigma-Aldrich; 0.01 mol) was added to distilled water (50 mL), and the solution was maintained under constant stirring for 5 min. Thereafter, calcium chloride dihydrate ($CaCl_2{\cdot}2H_2O$, Synth; 0.01 mol) was added, and the resulting solution was maintained under constant stirring for a further 5 min. Separately, a solution of potassium hydroxide (KOH, Vetec; 0.12 mol) in distilled water (20 mL) was prepared. The respective solutions were mixed and transferred to a polytetrafluoroethylene reaction cell, filling it to approximately 65% capacity. The cell was sealed, placed in a conventional microwave oven operating at a frequency of 2.45 Hz, and heated at a constant temperature of 140 °C and a base pressure of 2.5 bar for 10 min. The system temperature and pressure were monitored during the synthesis by means of a thermocouple and a manometer coupled to the reaction cell. The obtained material was washed with distilled water until the washings were neutral, and the powder was oven-dried at 100 °C for 12 h.

2.2. CTO-ZnS synthesis

For the heterostructure synthesis, two solutions were prepared. First, CTO (0.01 mol; obtained according to Section 2.1) was dispersed in ethylene glycol ($C_2H_6O_2$, EG, Synth; 25 mL). Simultaneously, a second solution was prepared by dispersing zinc nitrate hexahydrate ($Zn(NO_3)_2{\cdot}6H_2O$, Synth; 0.01 mol) and thiourea (CH_4N_2S, Synth; 0.03 mol) in EG (50 mL). The two solutions were mixed and transferred to a polytetrafluoroethylene reaction cell of capacity 110 mL. The cell was sealed, placed in a conventional microwave oven, heated at a rate of 5 °C/min to 180 °C, and maintained at this temperature for 32 min. The pressure and temperature were monitored throughout the synthesis. The resulting material was washed with distilled water until the washings were neutral, and the collected precipitate was oven-dried at 100 °C for 12 h. The preparation process of the CTO and CTO-ZnS heterostructure photocatalyst is shown schematically in Fig. 1.

2.3. Characterization techniques

The crystal structures of the CTO and CTO-ZnS powders were characterized by X-ray diffraction (XRD) analysis on a Shimadzu diffractometer model XRD 6000 (Shimadzu, Japan), employing Cu-K_α radiation and operated at 30 mA and 30 kV. The 2θ range from 10° to 80° was scanned, with a sampling step of 0.02° and a scanning speed of 2°/min. Raman spectra were acquired on a confocal Raman spectrometer (Voyage, BWTEK, USA) with an excitation wavelength of 785 nm and a spectral resolution of 3 cm^{-1}, operating at room temperature. Fourier-transform infrared (FTIR) spectra were acquired in the region 400–4000 cm^{-1} on an FTIR Prestige model 21 spectrometer (Shimadzu, Tokyo, Japan) equipped with a diamond crystal as an attenuated total reflectance device. The spectra were obtained in transmittance mode with a resolution of 4 cm^{-1}.

Diffuse-reflectance spectra were acquired on a UV/Vis spectrophotometer (Varian Cary 5000, USA) in the wavelength range 200–800 nm. Optical band gaps of the samples were estimated by the Tauc method for an indirect semiconductor, plotting $(\alpha h\nu)^{0.5}$ versus $h\nu$. The

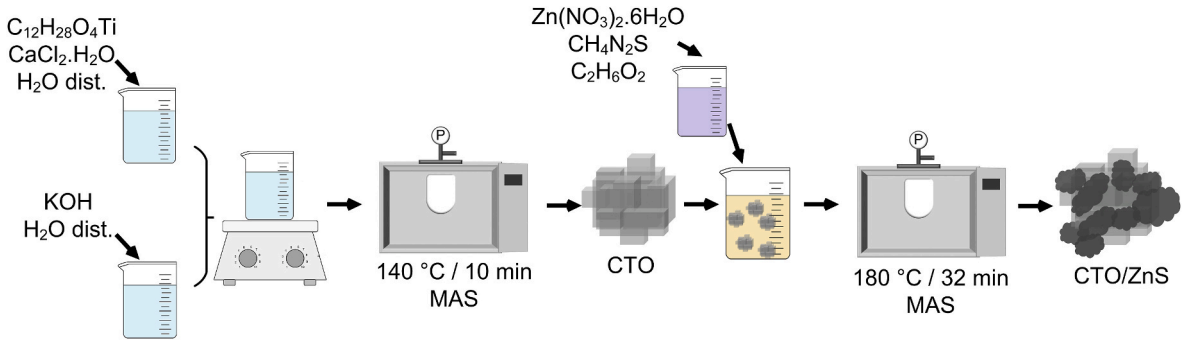

Fig. 1. Schematic illustration of the preparation of CTO and the CTO-ZnS photocatalyst.

photoluminescence (PL) of the samples was analyzed by means of a Thermal Jarrel-Ash Monospec monochromator and a Hamamatsu R446 photomultiplier. A krypton ion laser (Coherent Innova) with a wavelength of 405 nm was used as the excitation source, and the laser output was maintained at 200 mW. All measurements were taken at room temperature.

Scanning electron microscopy (SEM) images were obtained with a JSM-6610LV scanning electron microscope (JEOL, Japan) in high and low vacuum modes, with an energy-dispersive X-ray spectroscopy (EDX) microprobe operating at 15 kV. Transmission electron microscopy (TEM) analysis was performed on a JEM-2100F scanning electron microscope (JEOL, Japan) with a field emission gun (FEG) and an attachment for EDX, operating at 200 kV.

2.4. Photocatalytic activity

The photocatalytic activities of the samples in promoting the photooxidation of RhB dye ($C_{28}H_{31}ClN_2O_3$) in aqueous solution were tested under UVC illumination. First, catalyst powder (50 mg) was dispersed in 0.01 mM RhB solution (100 mL) and the samples were placed in a photoreactor at 25 °C under constant stirring. To avoid potential errors in adsorption results, the samples were pre-equilibrated by constant stirring in the dark for 10 min. Subsequently, the samples were illuminated by six UVC lamps (TUV Philips 15 W, giving 90 W in total), with maximum intensity at 254 nm. At 30 min intervals, aliquots (2 mL) were withdrawn and centrifuged at 3600 rpm for 5 min to separate the powder from the solution. The supernatant was subjected to UV/Vis analysis using a Bel Photonics spectrophotometer (model SP-2000 UV) to monitor the variation in the maximum absorption band of RhB.

Scavenger tests were performed using isopropyl alcohol (0.1 mM), ethylenediaminetetraacetic acid (0.5 mM), and $AgNO_3$ (0.5 mM) to suppress the action of hydroxyl radicals (HO^*), holes (h^+), and electrons (e^-), respectively.

In catalyst reuse tests, after the analysis each powder was separated by centrifugation and dried. The powders were then weighed and redeployed, maintaining the same ratio between catalyst (1 mg) and RhB solution (1 mL). The reuse process was carried out over five cycles.

3. Results and discussion

The XRD patterns of the CTO and CTO-ZnS samples are shown in Fig. 2 (a). It can be seen that the CTO sample showed an orthorhombic crystalline phase (*Pnma*) according to JCPDS PDF no. 22–153 [63]. Additionally, it was possible to verify the presence of a second $CaCO_3$ phase at $2\theta = 29°$, which is characteristic of this perovskite. The presence of $CaCO_3$ can be attributed to the use of water as the reaction medium and that calcium is part of the product composition. CO_2 dissolves in water, and the HCO_3^- ion readily interacts with calcium in hydrothermal/solvothermal reactions, generating the $CaCO_3$ phase. Moreover, titanium isopropoxide was used as a titanium precursor. This precursor has carbon in its composition, which also favors the formation of $CaCO_3$ during the synthesis process. Regarding the CTO-ZnS sample, it exhibited all of the characteristic peaks of CTO and a further broad peak between 27° and 30° attributable to ZnS, in accordance with JCPDS no. 5–566. The ZnS present in the sample had a cubic crystallographic phase, with the most intense peak (1 1 1) at $2\theta = 28°$. The fact that only the principal characteristic peak of ZnS is discernible may be due to its small amount on the heterostructure surface. According to some previous studies, the amount of precursor used in the sulfidation process influences the intensity of diffraction peaks of the cubic ZnS phase generated [64,65]. In the present study, it was observed that $CaCO_3$ disappeared when the CTO structure was covered with ZnS. The ZnS

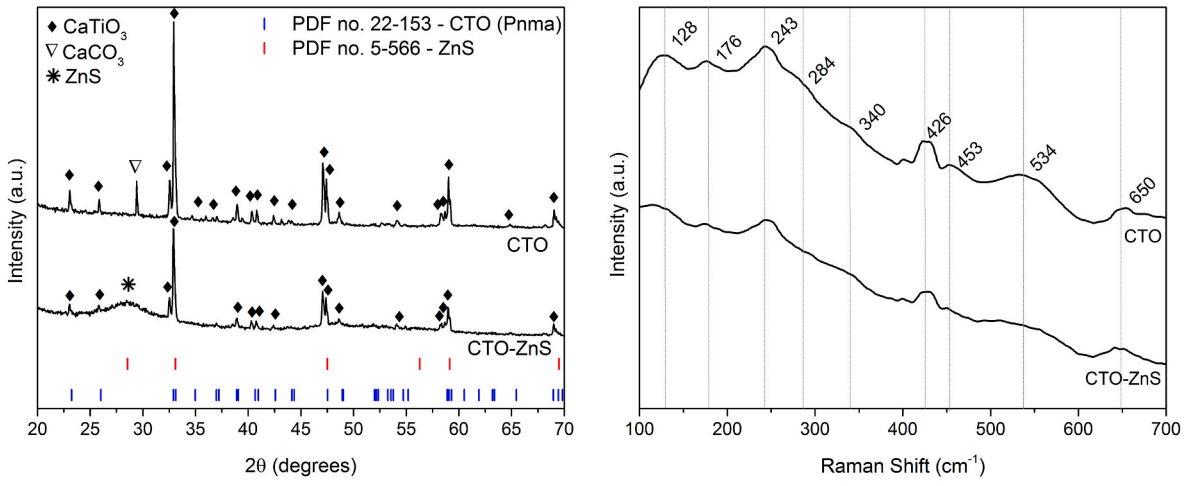

Fig. 2. (a) XRD patterns and (b) Raman spectra of CTO and CTO-ZnS samples synthesized by the microwave-assisted solvothermal method.

coating process was conducted at a higher temperature and for a longer duration (180 °C/32 min), providing more energy to the system, and consequently favoring the decomposition of $CaCO_3$. The modification of synthesis parameters to decrease the carbonate concentration in a perovskite has been reported previously [66]. In the XRD pattern of the CTO-ZnS heterostructure, all Bragg peaks of CTO appear at the same angles, indicating that modification with ZnS does not affect the structure of crystalline CTO nanoparticles.

The full-width at half-maximum (FWHM) of the three most intense peaks was used in Scherrer's equation, $D = 0.9\lambda/\beta\cos\theta$, to estimate the average crystallite size, D, of the samples, where λ is the XRD wavelength (0.15406 nm), β is the FWHM, and θ is the Bragg angle. CTO presented a crystallite size of 62.14 nm, whereas for the CTO-ZnS this value was 64.03 nm.

Fig. 2 (b) shows the Raman spectra of the CTO and CTO-ZnS samples. For both samples, it was possible to identify 9 10 vibrational modes, consistent with previous studies concerning CTO [18,51,57,67,68]. The vibrational mode at 128 cm^{-1} can be ascribed to the CTO lattice mode [68], and those at 176, 243, 284, and 340 cm^{-1} can be assigned as bending modes of O–Ti–O [51,57]. The peaks at 426, 453 and 534 cm^{-1} can be attributed to Ti–O_3 torsional modes, and that at 650 cm^{-1} can be assigned to a Ti–O symmetric stretching vibrational mode [18,51,67]. All listed peaks correspond exactly to the expected modes for the *Pnma* structure of CTO. It is important to note that, as expected, no Raman-active mode was identified for the cubic phase of the ZnS in the CTO-ZnS sample. When the structure is completely cubic, there are no Raman-active modes [69,70]. All vibrational modes of the CTO-ZnS sample were smoothed, consistent with successful covering.

The FTIR spectra of the CTO and CTO-ZnS samples are shown in Fig. 3. That of CTO features a small peak at 3450 cm^{-1}, assigned to the symmetric stretching vibration of –OH groups [71,72]. In the region around 3000 cm^{-1}, three weak absorption peaks are found, due to both asymmetric and symmetric C–H modes [72]. The strong peak at 1737 cm^{-1} can be attributed to the C═O stretching vibration [73], and that at 1447 cm^{-1} can be assigned to the bending vibration of CO_3^{2-} [71]. The peaks detected at 1365 and 1211 cm^{-1} can be ascribed to the bending mode of H–O–H and stretching vibration of C–OH, respectively [47,74,75]. The weak peak at 874 cm^{-1} can be assigned to the Ti–O stretching mode, which characteristically appears in the range 500–900 cm^{-1} [76]. The FTIR spectrum of CTO-ZnS features peaks distinct from those of CTO. The peaks at 3351 and 3185 cm^{-1} can be assigned to C–H stretching modes arising from the use of EG in the synthesis [77]. The peak at 2952 cm^{-1} corresponds to CH_3 asymmetric stretching, and those at 2915 and 2816 cm^{-1} correspond to CH_2 asymmetric and symmetric stretching modes, respectively [78]. A small difference in the spectrum can be discerned at around 2350 cm^{-1}, which can be ascribed to atmospheric CO_2 [79]. The peak at 2078 cm^{-1} can be ascribed to O═C═O stretching [80]. Stretching vibrations of C═O are observed at 1742 and 1621 cm^{-1}. The peak at 1417 cm^{-1} can be attributed to a Ca–Ti–O bond, and that at 1361 cm^{-1} is due to O–H deformation of a primary alcohol group [74]. Weak peaks in the region 1300–1000 cm^{-1} can be assigned to C═S vibrations [77]. The peak at 1045 cm^{-1} can be ascribed to the C–O stretching vibration mode of a primary alcohol [74]. The peak at 921 cm^{-1} can be assigned to interactions between the vibration modes of sulfide anions in the ZnS network [77]. Lastly, the peaks at 874 and 834 cm^{-1} can be attributed to Ti–O stretching modes, as observed in the spectrum of CTO [76].

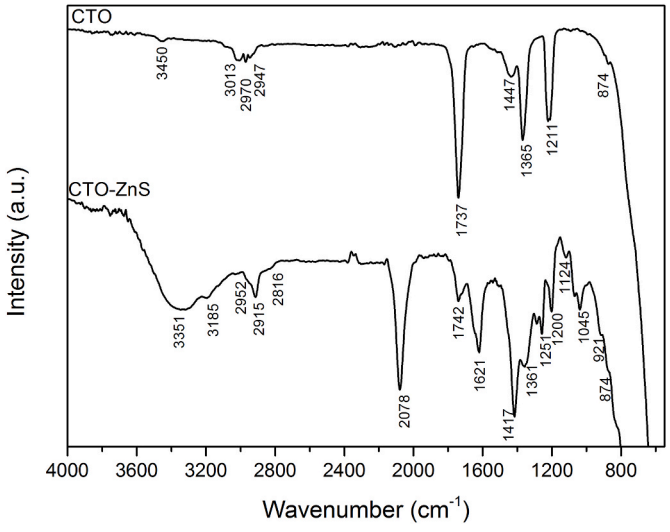

Fig. 3. FTIR spectra of the CTO and CTO-ZnS samples.

As shown in Fig. 4 (a) and (b), respectively, the band gaps of the CTO and CTO-ZnS samples were calculated by the Tauc model from the intercepts of tangents drawn to plots of $(\alpha h\nu)^{0.5}$ vs. $h\nu$, where α is the absorption coefficient and $h\nu$ is the photon energy in eV [81–83]. An appropriate relationship between the model and the data can be observed, resulting in R^2 values higher than 0.99 for both samples. In addition, CTO and CTO-ZnS showed the same band-gap value (3.58 eV), corresponding to a wavelength of 346 nm. It is worth mentioning that the band gap of the CTO obtained here is in accordance with values found in other works (around 3.5 eV) [51,57,84]; however, the value reported for ZnS is different (around 3.60 eV) [39,85]. Due to the similarity of the band gaps, no change in the value for the heterostructure with ZnS was perceivable.

Fig. 4 (c) shows photoluminescence curves for the CTO and CTO-ZnS samples, in which predominantly wide bands can be seen for both samples. This is characteristic when there are different intermediate levels in the band-gap energy resulting from relaxation processes [86–88]. This occurrence of intermediate, lower energy states can be explained by the contribution of the surface energies of the CTO and the ZnS thereon through the interaction between their respective CBs, in addition to the contribution of the interaction between the unfilled connections of the ZnS surface and the CTO surface. This leads to fewer energy transitions in the material, resulting in more emissions, and consequently reducing the distance that originates the intermediate states. The main peak for the CTO-ZnS heterostructure and the CTO is seen at 525 nm. It can be observed that the CTO-ZnS heterostructure had a higher PL intensity than the CTO, indicating that the superficial layer of ZnS had a great effect on the emission. The TEM images in Fig. 4 (further detailed in Fig. 6, along with the respective PL emission spectra of the samples), provide evidence of the importance of the ZnS surface layer on the CTO.

The CTO obtained by MAS is characterized by mesocrystals in the form of agglomerated microcubes, generated through the mechanism shown in Fig. 5 (a). To better illustrate this mechanism, Fig. 6 (a, c, and d) show SEM and TEM images of the CTO. Pereira et al. [56] demonstrated that the duration of MAS can influence the sample morphology; the longer the synthesis time, the more regular and cubic the CTO. To obtain CTO mesocrystals, a specific set of thermodynamic conditions (i.e., pressure and temperature), such as those implemented in this work, must be fulfilled [24]. Fig. 5 (b) shows the mechanism of formation of the ZnS particle cloud around the CTO. It is possible to follow the formation on the basis of the respective SEM and TEM images presented in Fig. 6 (e, g, and h).

Particle size was estimated from SEM images of the CTO, as exemplified by Fig. 6 (a), using Image J software. The CTO, which was composed of a cluster of cubic particles, had an average size of approximately 1.37 μm, as confirmed by TEM images, Fig. 6 (c, d).

When synthesizing CTO with ZnS, it was found that the latter did not form a covering ring on the former, but clouds of agglomerated particles around and over it, as indicated in Fig. 6 (e), evidencing heterostructure formation. In TEM images, it is possible to observe a large and dense CTO particle, and clouds of ZnS particles around it. This was confirmed by EDX analysis, Fig. 6 (f), which verified the presence of ZnS. As

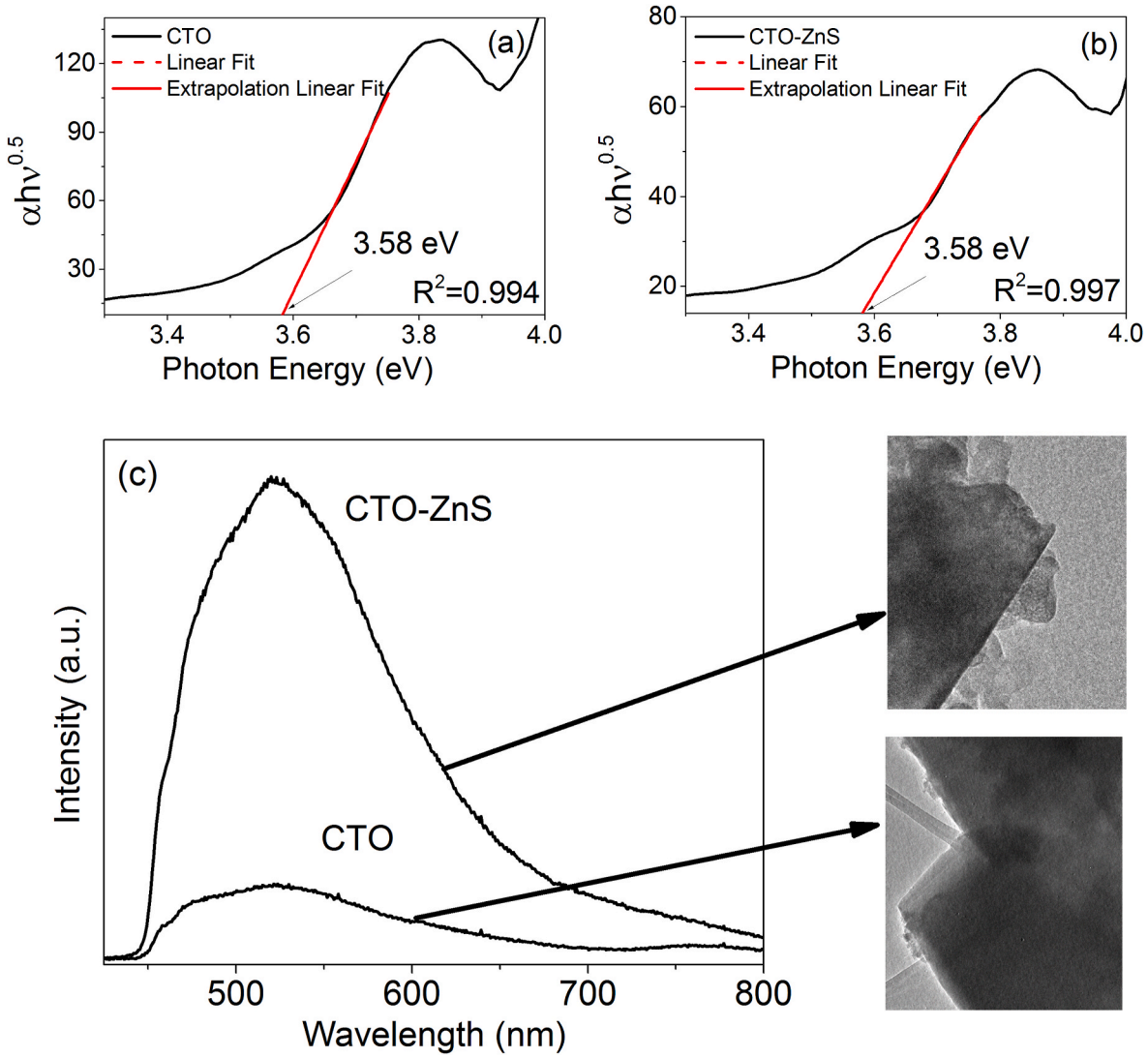

Fig. 4. Estimation of band-gap energies of (a) CTO and (b) CTO-ZnS heterostructure, and (c) PL emission spectra of both samples with the respective TEM images.

expected, the EDX pattern of the sample containing only CTO indicates the absence of ZnS-related peaks. As a CTO particle consists of a cluster of mesocrystals, the detected image has a higher density, making it difficult to visualize the ZnS present on the particle even though the surrounding particles indicate its presence on the CTO structure. This is corroborated by the TEM images in Fig. 6 (g, h), in which it can be seen that the CTO particle is largely covered by clouds of ZnS particles.

The particle size of the ZnS is difficult to estimate, as it does not have a defined shape. According to the SEM and TEM images, the ZnS particles are dispersed throughout the material and are much smaller than the CTO particles.

The photocatalytic activities of the CTO, ZnS, and CTO-ZnS heterostructure samples were tested in the degradation of RhB under UV radiation for a duration of 180 min. Fig. 7 displays the effect of the samples on the RhB concentration at intervals of 30 min, where C_0 is the initial concentration of the RhB dye solution and C is the RhB dye concentration at a given time. Fig. 7 (a) reveals that the CTO-ZnS achieved better results than the ZnS and CTO samples. The plot corresponding to the dye alone (without the addition of a semiconductor) is important to demonstrate that there was only slight natural discoloration over time, evidencing that the photocatalyst has an important effect on the process. ZnS alone showed a good discoloration ability compared to pure CTO. It can be noted that both ZnS and the heterostructure induced significant discoloration in the first hour of analysis, reaching equilibrium after this time. A plausible explanation for the greater photocatalytic discoloration facilitated by the samples containing ZnS may be physisorption of the dye on the surface of these materials [89,90]. In addition, the ZnS tends to lose most of its active sites during photocatalysis due to its rapid growth, requiring particle control to ensure an equilibrium during photocatalytic degradation [91].

We believe that the photocatalytic behavior of this system is affected by an intermediate level of order and disorder between the heterostructure interfaces. The structure of defects and density variation in the interface regions may be responsible for the different photocatalytic properties of systems based on heterostructures. After a photon with energy equal to or greater than the band gap of the semiconductor is absorbed, an electron/hole pair is generated on its surface. These charge carriers migrate to the catalytic surface, where the defect-free or defective surface and adsorbed oxygen molecules produce various species, such as peroxide ions (O_2^{2-}). Molecular oxygen reacts with CTO and ZnS species, resulting in more active species, thereby incorporating oxygen into the crystal lattice.

The Langmuir–Hinshelwood kinetic model was used to determine the reaction rate constant (k) of each sample in the photocatalytic discoloration process. Plots of $-\ln(C/C_0)$ as a function of time in Fig. 7 (b) reveal a good linear relationship, with $R^2 > 0.99$. This suggests that the photocatalytic degradation of the dye follows a pseudo-first-order process, expressed as $-\ln(C/C_0) = kt$, where t is the time in min. The k

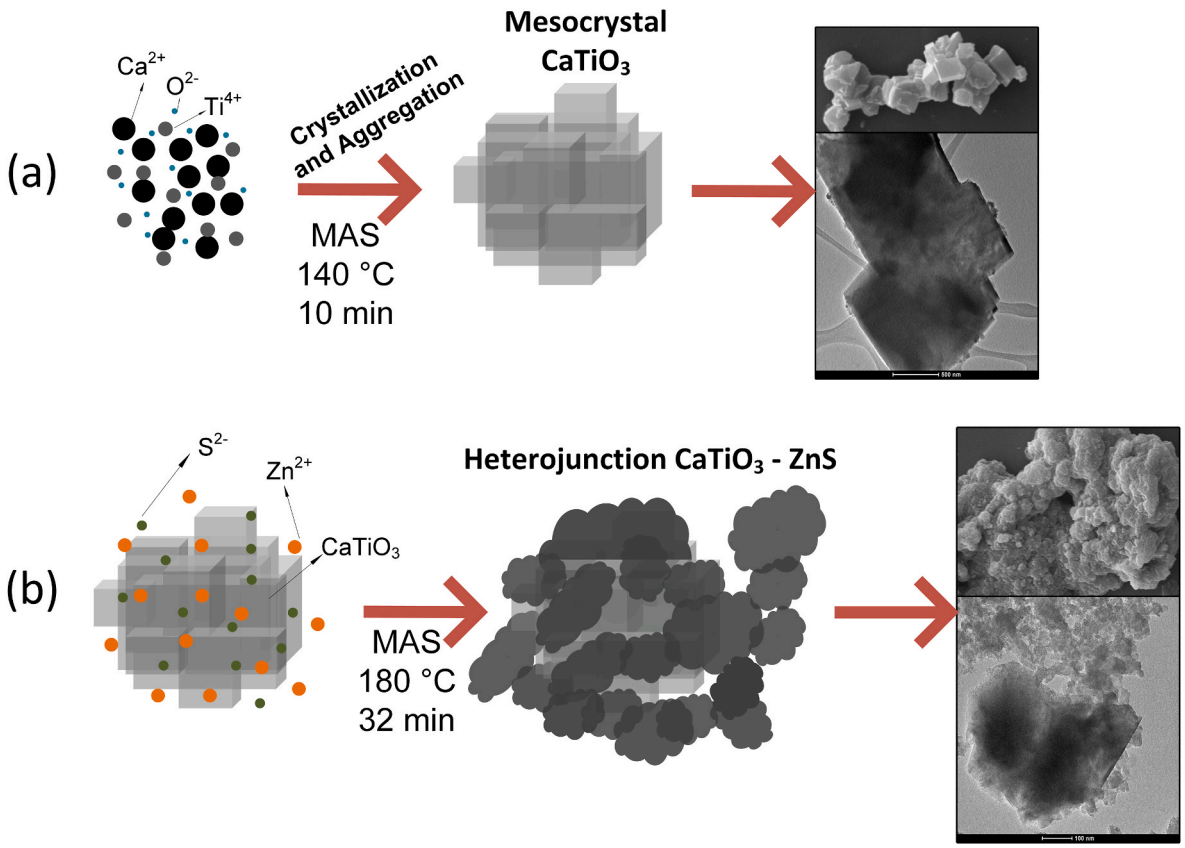

Fig. 5. Mechanism of CTO mesocrystal formation and CTO-ZnS heterostructure manufacture with the corresponding SEM and TEM images (shown in more detail in Fig. 6). (a) Formation of $CaTiO_3$ cubic mesocrystals. (b) Addition of ZnS particles onto the $CaTiO_3$ surface.

values shown in Fig. 7 (c) demonstrate that the heterostructure presented the highest value (0.01748), followed by ZnS (0.00946), and then CTO (0.00390), as compared to the blank of RhB without a catalyst (0.00087). These data indicate that the CTO-ZnS heterostructure is about 1.85, 4.48, and 19.4 times more efficient than pure ZnS, pure CTO, and the uncatalyzed system, respectively.

In terms of the extent of discoloration (Fig. 7 (d)), the heterostructure achieved 95.7% dye degradation in 180 min, whereas the ZnS and CTO samples achieved efficiencies of 81.8% and 50.5%, respectively. With the heterostructure and pure ZnS, 70% and 55%, respectively, of the dye degradation occurred in the first 60 min.

The improved photocatalytic activity of the CTO-ZnS heterostructure under UV irradiation in comparison with the pure samples can be ascribed to the combination of the respective semiconductors, both of which are capable of absorbing UV radiation, thus exciting electrons to the VB, mainly on surfaces with more disorder. This leads to the creation of some disordered surface states, which improves the photocatalysis of the material. These states are responsible for receiving electrons and confining photogenerated electrons, resulting in a more efficient transfer of charge carriers and preventing recombination, thus increasing the ability of the heterostructure to degrade the dye [92]. This was also demonstrated by PL analysis, as shown in Fig. 4 (c), whereby it was observed that the CTO-ZnS heterostructure led to more efficient photon–electron shocks and increased the electron density in the excited states and the number of holes in the VB.

The photocatalytic effects of the CTO-ZnS heterostructures with different proportions of ZnS were systematically compared, and the corresponding plots are displayed in the supplementary material (Fig. S1). Four different CTO:ZnS ratios (1:0.5, 1:1, 1:2, and 1:3) were tested. In Fig. S1, it can be seen that over 180 min of photocatalysis, the degradation efficiency of the sample with the highest proportion (1:3) tended to tail off before 180 min. However, after 180 min, the 1:1, 1:2, and 1:3 samples achieved the same % of RhB degradation, showing that the use of different proportions of CTO:ZnS did not influence the photocatalytic performance of the heterostructure.

Even though studies combining CTO and ZnS are still scarce in the literature, it is possible to find some works evaluating the respective individual materials. Kumar et al. [93] performed photocatalytic tests on a CTO heterostructure in combination with g-C_3N_4 under three different irradiation conditions, i.e., UV, visible, and sunlight, and found that regardless of the radiation used, the heterostructure showed the best photocatalytic performance. According to the authors, this improved photocatalytic activity was due to adequate band positions, as well as good interfacial contact of the two materials. In this work, we decided to test the photocatalytic degradation of the samples using only UV irradiation (254 nm), since the band gaps of both CTO and the CTO-ZnS heterostructure are in the UV range of the spectrum (3.58 eV). In the work by Han et al. [11], the photocatalytic degradation efficiency of CTO was tested under different heat treatments using methylene blue dye. The authors reported that CTO samples submitted to higher temperatures achieved greater efficiency. Additionally, when assessing the influence of different CTO synthesis strategies, which resulted in different particle shapes, they concluded that a sample synthesized by a solvothermal method gave the best dye degradation. It is worth mentioning that although the catalyst in this work was obtained by MAS synthesis, its particles consisted of cubes, whereas Han et al. [11] obtained CTO in the form of small spheres. According to these authors, it is possible to control the parameters of solvothermal synthesis in order to achieve different particle sizes, which can directly influence the photovoltaic response. Previous studies concerning CTO synthesis by the MAS method have also involved the generation of cubic particles after different synthesis times [51,56,67].

Based on the abovementioned results, it can be inferred that the combination of CTO and ZnS increases electron density, leading to an

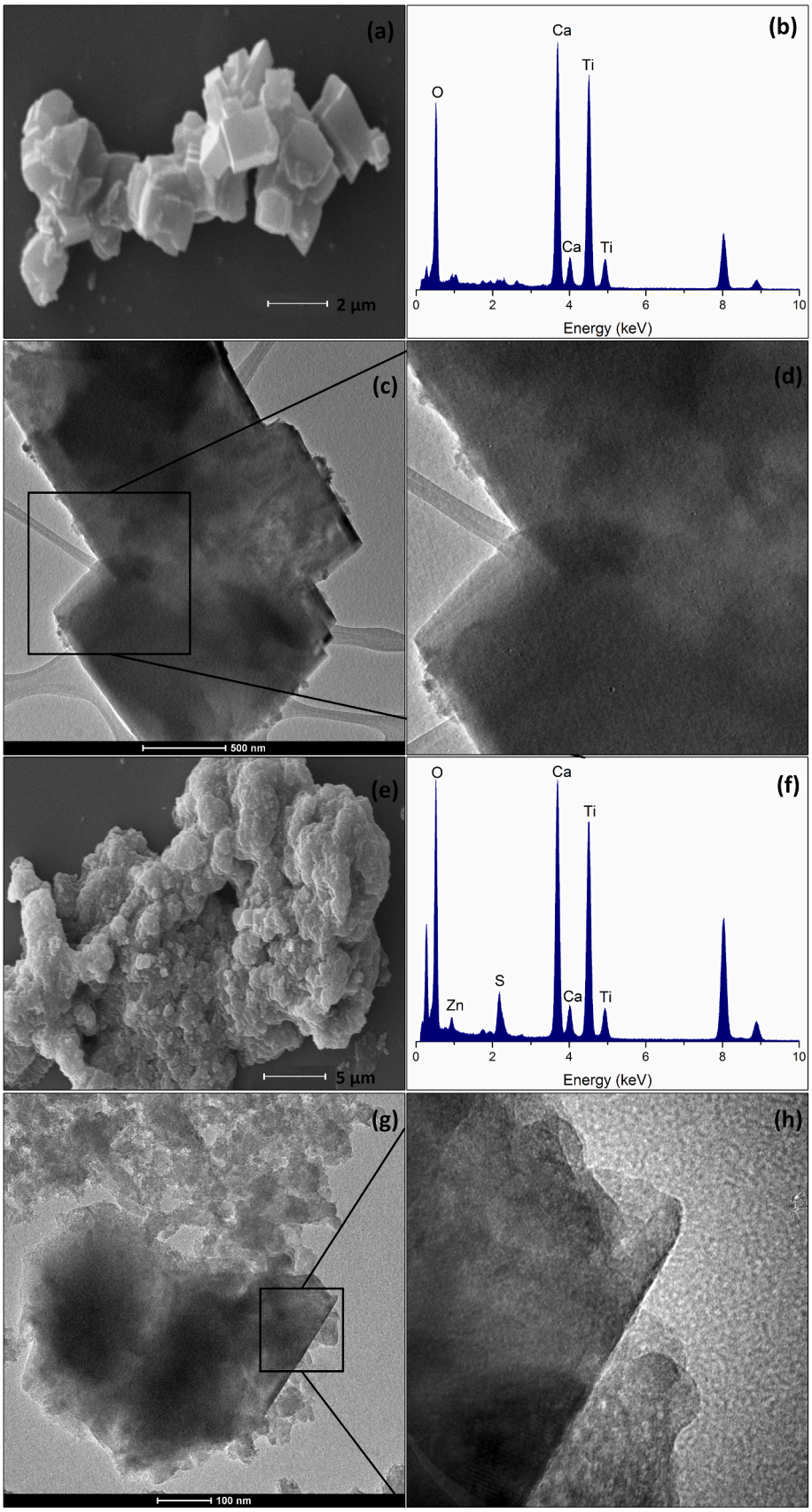

Fig. 6. Scanning electron microscopy images of (a) CTO and (e) CTO-ZnS samples; energy-dispersive X-ray patterns of (b) CTO and (f) CTO-ZnS samples; and transmission electron microscopy images of (c, d) CTO and (g, h) CTO-ZnS samples.

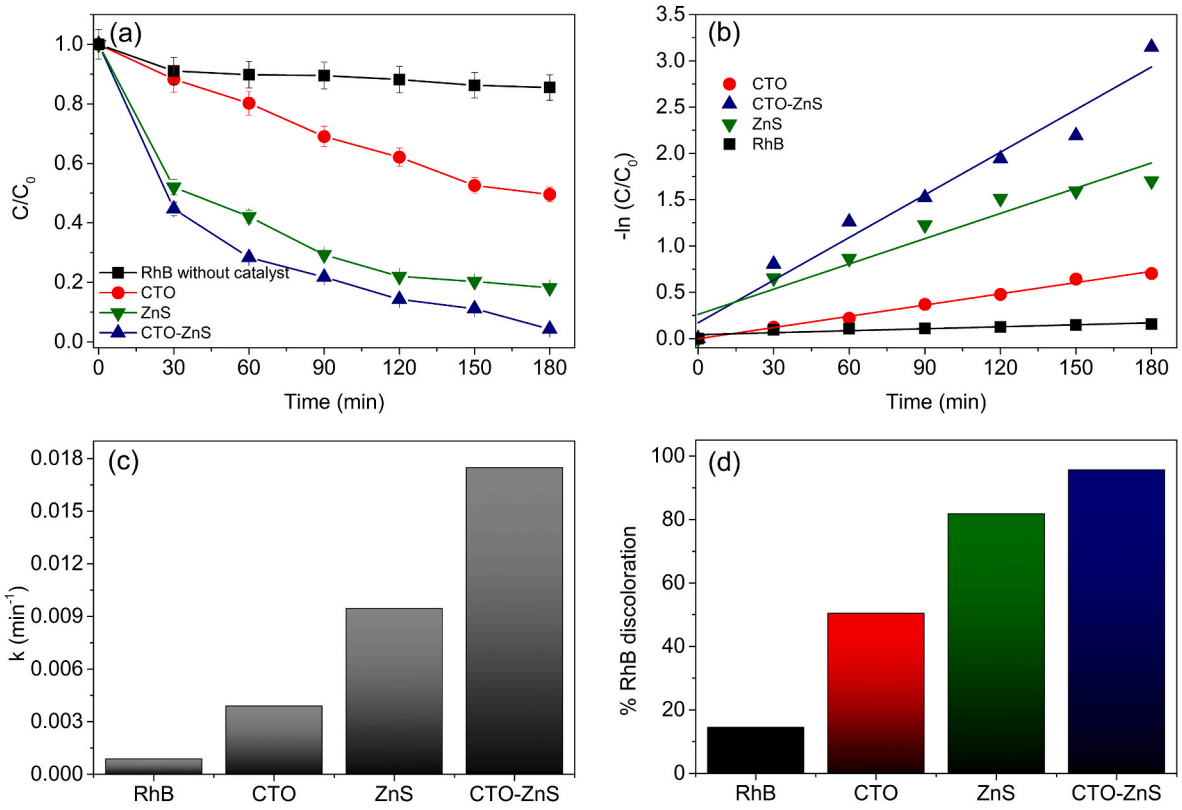

Fig. 7. (a) Time-dependent photocatalytic degradation of RhB over CTO, ZnS, and CTO-ZnS heterostructure under UV irradiation; (b) kinetic plots of dye degradation using the samples under UV irradiation; (c) pseudo-first-order rate constants (k) for the samples; (d) % of RhB discoloration over the respective samples after 180 min.

efficient transfer to O_2 and electron absorption by H_2O, ultimately generating HO_2^* and HO^*, thus enhancing the photodegradation performance of the material.

The proposed mechanism underpinning the photocatalytic activity of the heterostructure is elaborated below. First, to understand the photocatalytic mechanism it is necessary to know the VB and CB energy levels of the heterostructure components of CTO and ZnS. The formulae used to obtain E_{CB} and E_{VB} are as follows [93,94]:

$$E_{CB} = X - E_e - 0.5E_g \quad (1)$$

$$E_{VB} = E_{CB} + E_g \quad (2)$$

where E_{VB} and E_{CB} are the VB and CB edge potentials of the semiconductors, respectively, E_e is the energy of free electrons on the hydrogen scale (4.5 eV vs. NHE, normal hydrogen electrode), E_g is the band-gap energy of the semiconductor (3.58 eV for CTO and 3.7 eV for ZnS), and X is the average of absolute electronegativity (x) of each semiconductor atom ($x_{Ca} = 2.2$ eV, $x_{Ti} = 3.45$ eV, $x_O = 7.54$ eV, $x_{Zn} = 4.45$ eV, and $x_S = 6.22$ eV) [95]. The X value for each semiconductor was evaluated as follows [94,96]:

$$X(CaTiO_3) = \left(x_{Ca} \times x_{Ti} \times x_O^3\right)^{1/5} \quad (3)$$

$$X(ZnS) = \left(x_{Zn} \times x_S\right)^{1/2} \quad (4)$$

After assigning the respective values in the above formulae, the values of $X(CaTiO_3)$ and $X(ZnS)$ were determined as 5.04 eV and 5.26 eV, respectively. Based on this information, the calculated E_{CB} values for CTO and ZnS are −1.25 eV and −1.09 eV vs. NHE, respectively, and the E_{VB} values are 2.33 eV and 2.61 eV, respectively.

As the heterostructure is formed by covering the CTO structure with ZnS (both n-type semiconductors), there are changes in the charge-transfer process. The CB of ZnS has a more positive potential (vs. NHE) than that of CTO, whereas the VB of CTO is more negative (vs. NHE) than that of ZnS, as shown in Fig. 8. The MAS method increases the semiconductor character by creating a higher order/disorder density between the clusters of the two compounds. When photons ($h\nu$) with energy equal to or greater than the CTO-ZnS band gap impinge upon the heterostructure surface, electron/hole ($e'/h^\bullet$) pairs are generated according to Eq. (5). The coating material (ZnS) has a larger band gap, causing the photogenerated electrons to migrate from the CB of the ZnS to the CB of the material present in the nucleus (CTO). Meanwhile, holes migrate from the VB of the CTO to the VB of the ZnS through the heterostructure interface [Eqs. (6) and (7)] [42,97–100]. It has been

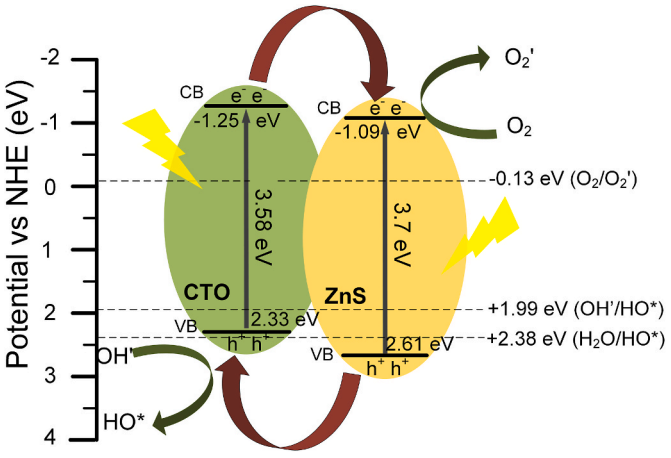

Fig. 8. Proposed band structure scheme involving the CTO-ZnS heterostructure.

reported that electrons reduce adsorbed oxygen to the superoxide radical ($O_2^{'}$) [Eq. (9)] [47,93] and that the formation of this radical is facilitated since the reduction potential of $O_2/\ O_2^{'}$ is −0.13 eV vs. NHE; this value is more negative than the CB edge potential of the CTO (−1.25 eV) [101]. The hole in the VB reacts with $OH^{'}$ ions to form HO^{*} and $H^{\bullet}$ radicals [Eq. (8)] due to its more positive potential than $OH^{'}/\ HO^{*}$ (1.99 eV vs. NHE) [93,94]. Regarding the H_2O potential, the CTO has a less positive VB (2.33 eV) than the $H_2O/\ HO^{*}$ potential (2.38 eV vs. NHE), suggesting that it cannot couple to H_2O to produce HO^{*} radicals [101]. In contrast, the VB of the ZnS (2.61 eV) is more positive than the $H_2O/\ HO^{*}$ potential, indicating that it can react with H_2O species to produce HO^{*} radicals.

The active species are then formed through the superoxide radical, whereby $O_2^{'}$ reacts with $H^{\bullet}$ in solution to form the hydroperoxyl radical (HO_2^{*}), which in turn is converted into hydrogen peroxide (H_2O_2) [Eqs. (10) and (11)]. It is important to mention that this H_2O_2 can produce both HO^{*} and $OH^{\bullet}$ [Eq. (12)]. RhB reacts with active species, such as HO_2^{*} and HO^{*}, being degraded into intermediate products according to Eq. (13). The semiconductors serve both to transport the electron to oxygen in an exothermic reaction and to break the O–H bond of water by absorbing an electron in the VB of the semiconductor in an endothermic reaction.

$$CTO\ /\ ZnS + h\nu \rightarrow CTO\ /\ ZnS + e^{'}_{(CB)} + h^{\bullet}_{(VB)} \quad (5)$$

$$CTO\ /\ ZnS\left(e^{'}_{(CB)}\right) \rightarrow CTO\ \left(e^{'}_{(CB)}\right)\ /\ ZnS \quad (6)$$

$$CTO\left(h^{\bullet}_{(VB)}\right)\ /\ ZnS \rightarrow CTO\ /\ ZnS\ \left(h^{\bullet}_{(VB)}\right) \quad (7)$$

$$h^{\bullet}_{(VB)} + H_2O \rightarrow HO^{*} + H^{\bullet} \quad (8)$$

$$e^{'}_{(CB)} + O_{2_{ads}} \rightarrow O_2^{'} \quad (9)$$

$$O_2^{'} + H^{\bullet} \rightarrow HO_2^{*} \quad (10)$$

$$2HO_2^{*} \rightarrow O_2 + H_2O_2 \quad (11)$$

$$H_2O_2 + e^{'}_{(CB)} \rightarrow HO^{*} + OH^{\bullet} \quad (12)$$

$$RhB + HO_2^{*} + HO^{*} \rightarrow \text{degradation products} \quad (13)$$

The scavenger methodology was applied to the photocatalytic mechanism in order to identify the main active species operative. Fig. 9 shows plots of RhB dye concentration as a function of assay time in the presence of charge scavengers. To identify the active species in the photocatalytic process, isopropyl alcohol (C_3H_8O), silver nitrate ($AgNO_3$), and disodium ethylenediaminetetraacetate (EDTA) were used as scavengers for HO^{*}, e^{-}, and h^{+}, respectively. Fig. 9 (a) displays the plots for the CTO sample. It can be observed that the use of EDTA scavenger caused a decrease in the photocatalytic RhB degradation efficiency, suggesting that h^{+} plays an important role in the oxidation of RhB. Since the addition of isopropyl alcohol slightly increased the degradation of RhB in the last hour of analysis, it can be concluded that hydroxyl radicals were not the main species operative in the photocatalytic mechanism. Although $AgNO_3$ greatly increased dye adsorption, it also inhibited the photocatalytic activity of CTO. In addition, the use of $AgNO_3$ suppressed e^{-} recombination with h^{+}. As a result, e^{-} became available to act in the photocatalytic process, consequently increasing the degradation ability of the sample. This implicates both e^{-} and h^{+} as principal active species in the photocatalysis. In Fig. 9 (b) and (c), corresponding to the CTO-ZnS and ZnS samples, respectively, it is possible to observe that even though the addition of scavengers provided an increase in the dye adsorption on the heterostructure surface, it also inhibited the photocatalytic degradation of the material, demonstrating that e^{-}, h^{+} and HO^{*} were the main species acting in the photocatalytic process.

Fig. 10 shows the results of cyclic tests of RhB degradation over 180 min for the CTO-ZnS, CTO, and ZnS samples. Reuse tests are important to determine the chemical stability of the material during repeated photocatalytic cycles. After five successive cycles, the samples maintained consistent photocatalytic efficiency without apparent deactivation, indicating that the pure CTO, pure ZnS, and CTO-ZnS heterostructure were stable during the degradation process. In addition, the heterostructure recovered after the five cycles was characterized by XRD, as shown in Fig. S2 of the supplementary material. No noticeable changes were observed after the stability test, evidencing that the CTO-ZnS heterostructure has high stability.

4. Conclusion

Microwave-assisted solvothermal synthesis has been proved to be a favorable method for obtaining CTO and a CTO-ZnS heterostructure due to its versatility, simplicity, and rapidity for synthesizing nanoparticulate materials. The CTO-ZnS heterostructure obtained by the MAS method showed vastly superior results in RhB dye degradation than pure CTO synthesized by the same method. Specifically, it achieved 95% RhB degradation in 180 min under UVC irradiation, as compared to just 53% over pure CTO. The cloud of ZnS particles formed around the CTO structure favors physisorption of the dye on the semiconductor surface. Furthermore, the formation of disordered surface states at the heterojunction expedites charge transfer, thus increasing the ability of the material to degrade RhB. These results suggest that it is possible to obtain a CTO-ZnS heterostructure through a simple and rapid MAS synthesis method. Moreover, the cloud of ZnS particles around CTO increases the dye photodiscoloration capacity of the material, thus contributing to studies on photocatalytic processes aimed at removing pollutants from effluents.

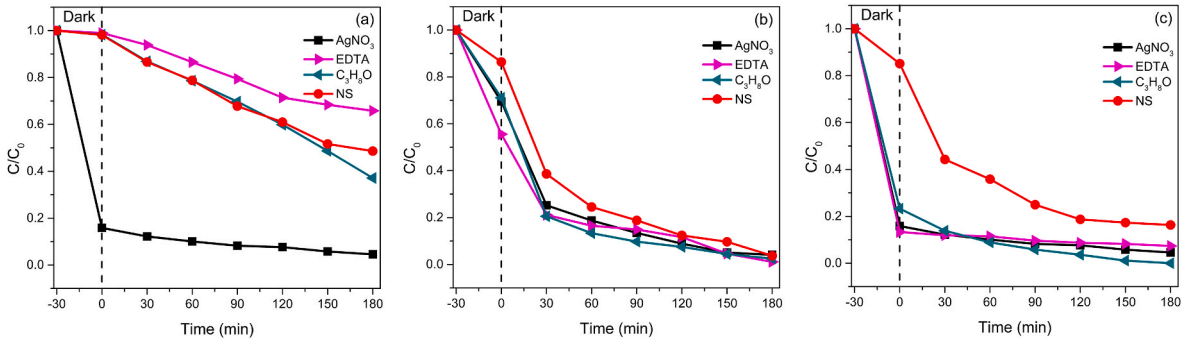

Fig. 9. Plots of RhB dye degradation in the presence of isopropyl alcohol (C_3H_8O), silver nitrate ($AgNO_3$), and EDTA as scavengers, along with those without scavengers, for (a) CTO, (b) CTO-ZnS, and (c) ZnS samples.

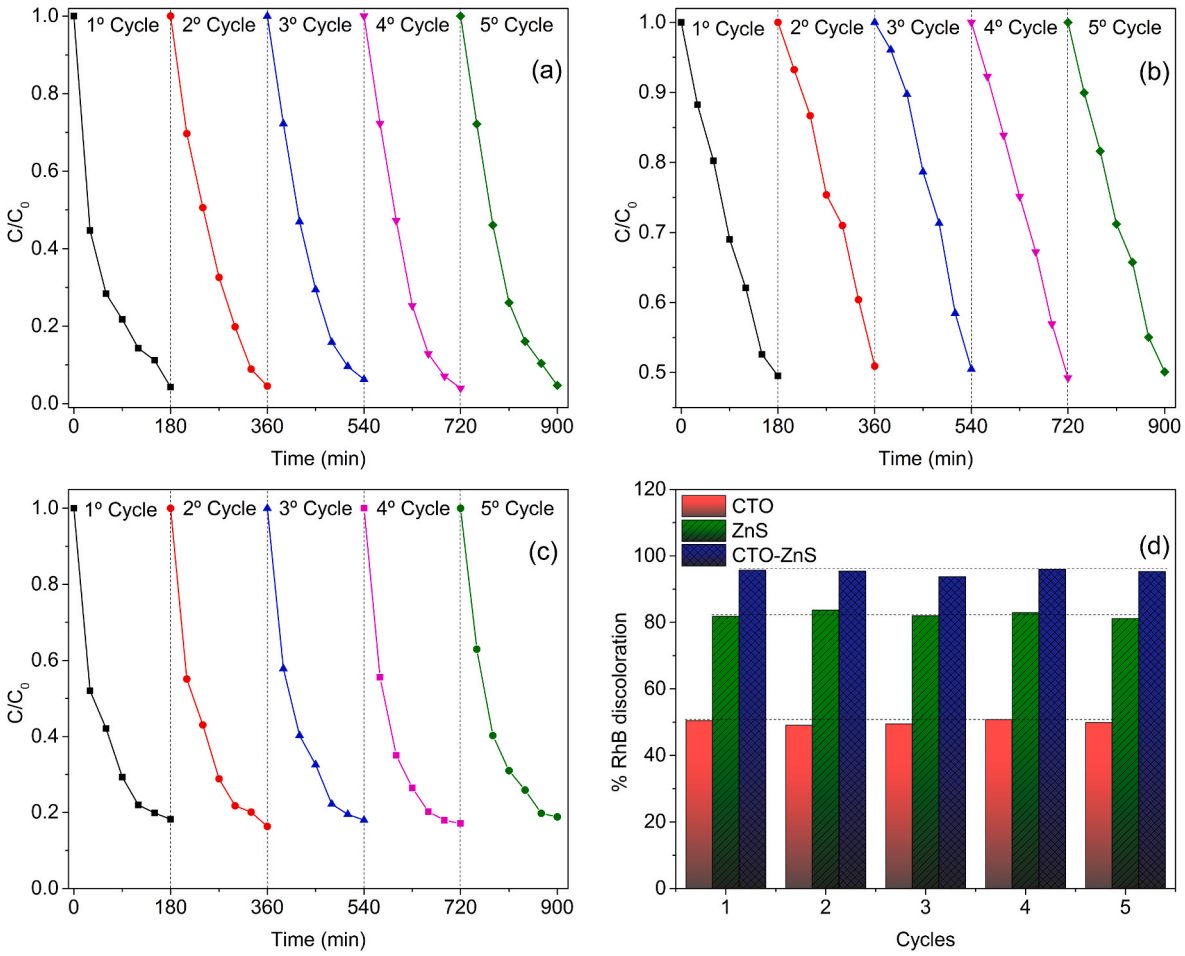

Fig. 10. Recycling performances of the samples towards RhB degradation: (a) CTO-ZnS, (b) CTO, (c) ZnS, and (d) % of RhB discoloration over the respective samples.

CRediT author statement

Cátia L. Ücker: Conceptualization, Methodology, Software, Investigation, Data curation, Writing - Original Draft. **Suelen R. Almeida:** Methodology, Investigation, Validation, Writing - Original Draft. **Renato G. Cantoneiro:** Methodology, Validation. **Lisiane O. Diehl:** Methodology, Validation. **Sergio Cava:** Writing - Review & Editing, Funding acquisition. **Mario L. Moreira:** Writing - Review & Editing. **Elson Longo:** Resources, Funding acquisition. **Cristiane W. Raubach:** Writing - Review & Editing, Supervision, Project administration.

Declaration of competing interest

The authors declare that they have no known competing financial interests or personal relationships that could have appeared to influence the work reported in this paper.

Data availability

Data will be made available on request.

Acknowledgments

The authors are thankful for the financial support of the following Brazilian research funding agencies: CAPES, CNPq, and FAPERGS – Processes 17/25510000889-8 and 19/2551-0001974-2. We also thank the CEME-SUL FURG and Unipampa/PROPESQ. This study was partly financed by the Coordenação de Aperfeiçoamento de Pessoal de Nível Superior–Brasil (CAPES) – Finance Code 001.

Appendix A. Supplementary data

Supplementary data to this article can be found online at https://doi.org/10.1016/j.jpcs.2022.111050.

References

[1] B.M. Bresolin, Y. Park, D.W. Bahnemann, Recent progresses on metal halide perovskite-based material as potential photocatalyst, Catalysts 10 (2020) 1–34, https://doi.org/10.3390/catal10060709.

[2] B. Szczepanik, Photocatalytic degradation of organic contaminants over clay-TiO_2 nanocomposites: a review, Appl. Clay Sci. 141 (2017) 227–239, https://doi.org/10.1016/j.clay.2017.02.029.

[3] H. Ashiq, N. Nadeem, A. Mansha, J. Iqbal, M. Yaseen, M. Zahid, I. Shahid, G-C3N4/Ag@CoWO4: a novel sunlight active ternary nanocomposite for potential photocatalytic degradation of rhodamine B dye, J. Phys. Chem. Solid. 161 (2022), 110437, https://doi.org/10.1016/j.jpcs.2021.110437.

[4] F.F. Brites, V.S. Santana, N.R.C. Fernandes-Machado, Effect of support on the photocatalytic degradation of textile effluents using Nb_2O_5 and ZnO: photocatalytic degradation of textile dye, Top. Catal. 54 (2011) 264–269, https://doi.org/10.1007/s11244-011-9657-2.

[5] O.M. Rodriguez-Narvaez, J.M. Peralta-Hernandez, A. Goonetilleke, E.R. Bandala, Treatment technologies for emerging contaminants in water: a review, Chem. Eng. J. 323 (2017) 361–380, https://doi.org/10.1016/j.cej.2017.04.106.

[6] A.O. Ibhadon, P. Fitzpatrick, Heterogeneous photocatalysis: recent advances and applications, Catalysts 3 (2013) 189–218, https://doi.org/10.3390/catal3010189.

[7] M. Cheng, G. Zeng, D. Huang, C. Lai, P. Xu, C. Zhang, Y. Liu, Hydroxyl radicals based advanced oxidation processes (AOPs) for remediation of soils contaminated with organic compounds: a review, Chem. Eng. J. 284 (2016) 582–598, https://doi.org/10.1016/j.cej.2015.09.001.

[8] F. Kiriakidou, D.I. Kondarides, X.E. Verykios, The effect of operational parameters and TiO_2-doping on the photocatalytic degradation of azo-dyes, Catal. Today 54 (1999) 119–130, https://doi.org/10.1016/S0920-5861(99)00174-1.

[9] M.A. Peña, J.L.G. Fierro, Chemical structures and performance of perovskite oxides, Chem. Rev. 101 (2001) 1981, https://doi.org/10.1021/cr980129f. –2017.

[10] W. Janosik, C.A. Randall, M. Lanagan, Thermodynamic and electrical effects of residual carbon in glass-barium titanate composites for MLCC applications, J. Am. Ceram. Soc. 90 (2007) 2415–2419, https://doi.org/10.1111/j.1551-2916.2007.01748.x.

[11] C. Han, J. Liu, W. Yang, Q. Wu, H. Yang, X. Xue, Photocatalytic activity of $CaTiO_3$ synthesized by solid state, sol–gel and hydrothermal methods, J. Sol. Gel Sci. Technol. 81 (2017) 806–813, https://doi.org/10.1007/s10971-016-4261-3.

[12] J. Zhuang, Q. Tian, S. Lin, W. Yang, L. Chen, P. Liu, Precursor morphology-controlled formation of perovskites $CaTiO_3$ and their photo-activity for As(III) removal, Appl. Catal. B Environ. (2014) 156–157, https://doi.org/10.1016/j.apcatb.2014.02.015, 108–115.

[13] F. Zhao, Z. Yue, J. Pei, H. Zhuang, Z. Gui, L. Li, Structure and microwave dielectric properties of hexagonal $Ba[Ti_{1-x}(Ni_{1/2}W_{1/2})_x]O_3$ ceramics, J. Am. Ceram. Soc. 90 (2007) 2461–2466, https://doi.org/10.1111/j.1551-2916.2007.01801.x.

[14] K.V. Karthik, C.V. Reddy, K.R. Reddy, R. Ravishankar, G. Sanjeev, R.V. Kulkarni, N.P. Shetti, A.V. Raghu, Barium titanate nanostructures for photocatalytic hydrogen generation and photodegradation of chemical pollutants, J. Mater. Sci. Mater. Electron. 30 (2019) 20646–20653, https://doi.org/10.1007/s10854-019-02430-6.

[15] U.O. Bhagwat, J.J. Wu, A.M. Asiri, S. Anandan, Synthesis of $MgTiO_3$ nanoparticles for photocatalytic applications, ChemistrySelect 4 (2019) 788–796, https://doi.org/10.1002/slct.201803583.

[16] L. Boudjellal, A. Belhadi, R. Brahimi, S. Boumaza, M. Trari, Semiconducting and photoelectrochemical properties of the ilmenite $CoTiO_3$ prepared by wet method and its application for O_2 evolution under visible light, J. Solid State Electrochem. 24 (2020) 357–364, https://doi.org/10.1007/s10008-019-04464-6.

[17] B.L. Phoon, C.W. Lai, J.C. Juan, P.L. Show, G.T. Pan, Recent developments of strontium titanate for photocatalytic water splitting application, Int. J. Hydrogen Energy 44 (2019) 14316–14340, https://doi.org/10.1016/j.ijhydene.2019.01.166.

[18] L.S. Cavalcante, V.S. Marques, J.C. Sczancoski, M.T. Escote, M.R. Joya, J. A. Varela, M.R.M.C. Santos, P.S. Pizani, E. Longo, Synthesis, structural refinement and optical behavior of $CaTiO_3$ powders: a comparative study of processing in different furnaces, Chem. Eng. J. 143 (2008) 299–307, https://doi.org/10.1016/j.cej.2008.05.017.

[19] V.V. Shanbhag, S.C. Prashantha, H. Nagabhushana, D.M. Jnaneshwara, N. Basavaraju, H.P. Nagaswarupa, K.M. Girish, R. Naik, Impacts of core shell structure on structural and photoluminescence properties of $CaTiO_3:Sm^{3+}$, Li^+ nanoparticles for solid-state display applications, Mater. Res. Express 6 (2019), 085037, https://doi.org/10.1088/2053-1591/ab1d1d.

[20] H. Zhang, G. Chen, X. He, J. Xu, Electronic structure and photocatalytic properties of Ag-La co-doped $CaTiO_3$, J. Alloys Compd. 516 (2012) 91–95, https://doi.org/10.1016/j.jallcom.2011.11.142.

[21] H. Mizoguchi, K. Ueda, M. Orita, S.C. Moon, K. Kajihara, M. Hirano, H. Hosono, Decomposition of water by a $CaTiO_3$ photocatalyst under UV light irradiation, Mater. Res. Bull. 37 (2002) 2401–2406, https://doi.org/10.1016/S0025-5408(02)00974-1.

[22] J. Han, Y. Liu, F. Dai, R. Zhao, L. Wang, Fabrication of CdSe/$CaTiO_3$ nanocomposites in aqueous solution for improved photocatalytic hydrogen production, Appl. Surf. Sci. 459 (2018) 520–526, https://doi.org/10.1016/j.apsusc.2018.08.026.

[23] R. Chen, D. Chen, Enhanced luminescence properties of $CaTiO_3:Pr^{3+}$ phosphor with addition of SiO_2 by solid-state reaction, Spectrochim. Acta Part A Mol. Biomol. Spectrosc. 127 (2014) 256–260, https://doi.org/10.1016/j.saa.2014.02.046.

[24] M.L. Moreira, J.R. Bordin, J. Andrés, J.A. Varela, E. Longo, A description of the formation and growth processes of $CaTiO_3$ mesocrystals: a joint experimental and theoretical approach, Mol. Syst. Des. Eng. (2020), https://doi.org/10.1039/D0ME00043D. MSDE.

[25] S. Otsuka-Yao-Matsuo, T. Omata, S. Ueno, M. Kita, Photobleaching of Methylene Blue aqueous solution sensitized by composite powders of titanium oxide with $SrTiO_3$, $BaTiO_3$, and $CaTiO_3$, Mater. Trans. 44 (2003) 2124–2129, https://doi.org/10.2320/matertrans.44.2124.

[26] Y.X. Yan, H. Yang, Z. Yi, T. Xian, R.S. Li, X.X. Wang, Construction of Ag_2S@$CaTiO_3$ heterostructure photocatalysts for enhanced photocatalytic degradation of dyes, Desalination Water Treat. 170 (2019) 349–360, https://doi.org/10.5004/dwt.2019.24747.

[27] P. Reiss, M. Protière, L. Li, Core/shell semiconductor nanocrystals, Small 5 (2009) 154–168, https://doi.org/10.1002/smll.200800841.

[28] S. Bera, N. Pradhan, Perovskite nanocrystal heterostructures: synthesis, optical properties, and applications, ACS Energy Lett. 5 (2020) 2858–2872, https://doi.org/10.1021/acsenergylett.0c01449.

[29] A. Enesca, L. Andronic, The influence of photoactive heterostructures on the photocatalytic removal of dyes and pharmaceutical active compounds: a mini-review, Nanomaterials 10 (2020) 1–22, https://doi.org/10.3390/nano10091766.

[30] S. Das, J. Pérez-Ramírez, J. Gong, N. Dewangan, K. Hidajat, B.C. Gates, S. Kawi, Core-shell structured catalysts for thermocatalytic, photocatalytic, and electrocatalytic conversion of CO_2, Chem. Soc. Rev. 49 (2020) 2937–3004, https://doi.org/10.1039/c9cs00713j.

[31] C.W. Raubach, Y.V.B. De Santana, M.M. Ferrer, V.M. Longo, J.A. Varela, W. Avansi, P.G.C. Buzolin, J.R. Sambrano, E. Longo, Structural and optical approach of CdS@ZnS core-shell system, Chem. Phys. Lett. 536 (2012) 96–99, https://doi.org/10.1016/j.cplett.2012.03.090.

[32] M. Jothibas, C. Manoharan, S.J. Jeyakumar, P. Praveen, I.K. Punithavathy, J. P. Richard, Synthesis and enhanced photocatalytic property of Ni-doped ZnS nanoparticles, Sol. Energy 159 (2018) 434–443, https://doi.org/10.1016/j.solener.2017.10.055.

[33] X. Wang, H. Huang, B. Liang, Z. Liu, D. Chen, G. Shen, ZnS nanostructures: synthesis, properties, and applications, Crit. Rev. Solid State Mater. Sci. 38 (2013) 57–90, https://doi.org/10.1080/10408436.2012.736887.

[34] X. Fang, T. Zhai, U.K. Gautam, L. Li, L. Wu, Y. Bando, D. Golberg, ZnS nanostructures: from synthesis to applications, Prog. Mater. Sci. 56 (2011) 175–287, https://doi.org/10.1016/j.pmatsci.2010.10.001.

[35] H. Bagheri, M. Akbarzadeh Pasha, M. Mansour Lakouraj, Synthesis, physicochemical properties and antibacterial activity of hybrid nanocomposite of ZnS nanoparticles-decorated GO@CS, Phys. Scripta 95 (2020), https://doi.org/10.1088/1402-4896/abaad4.

[36] G.R. Amir, S. Fatahian, N. Kianpour, Investigation of ZnS nanoparticle antibacterial effect, Curr. Nanosci. 10 (2014) 796–800, https://doi.org/10.2174/1573413710666140604220007.

[37] K.S. Ranjith, A. Senthamizhan, B. Balusamy, T. Uyar, Nanograined surface shell wall controlled ZnO-ZnS core-shell nanofibers and their shell wall thickness dependent visible photocatalytic properties, Catal. Sci. Technol. 7 (2017) 1167–1180, https://doi.org/10.1039/c6cy02556k.

[38] S. Arjunan, H.P. Kavitha, S. Ponnusamy, N. Mani, Y. Hayakawa, ZnS/CuS nanocomposites: an effective strategy to transform UV-active ZnS to UV and Vis light-active ZnS, J. Mater. Sci. Mater. Electron. 27 (2016) 9022–9033, https://doi.org/10.1007/s10854-016-4935-1.

[39] M. Sookhakian, Y.M. Amin, W.J. Basirun, M.T. Tajabadi, N. Kamarulzaman, Synthesis, structural, and optical properties of type-II ZnO-ZnS core-shell nanostructure, J. Lumin. 145 (2014) 244–252, https://doi.org/10.1016/j.jlumin.2013.07.032.

[40] N.S. Kozhevnikova, M.A. Melkozerova, A.N. Enyashin, A.P. Tyutyunnik, L. A. Pasechnik, I.V. Baklanova, A.Y. Suntsov, A.A. Yushkov, L.Y. Buldakova, M. Y. Yanchenko, Janus ZnS nanoparticles: synthesis and photocatalytic properties, J. Phys. Chem. Solid. 161 (2022), 110459, https://doi.org/10.1016/j.jpcs.2021.110459.

[41] L. Yu, W. Chen, D. Li, J. Wang, Y. Shao, M. He, P. Wang, X. Zheng, Inhibition of photocorrosion and photoactivity enhancement for ZnO via specific hollow ZnO core/ZnS shell structure, Appl. Catal. B Environ. 164 (2015) 453–461, https://doi.org/10.1016/j.apcatb.2014.09.055.

[42] N. Qutub, B.M. Pirzada, K. Umar, O. Mehraj, M. Muneer, S. Sabir, Synthesis, characterization and visible-light-driven photocatalysis by differently structured CdS/ZnS sandwich and core-shell nanocomposites, Phys. E Low-Dimensional Syst. Nanostructures. 74 (2015) 74–86, https://doi.org/10.1016/j.physe.2015.06.023.

[43] S. Mathew, B.S. Bhardwaj, A.D. Saran, P. Radhakrishnan, V.P.N. Nampoori, C.P. G. Vallabhan, J.R. Bellare, Effect of ZnS shell on optical properties of CdSe-ZnS core-shell quantum dots, Opt. Mater. 39 (2015) 46–51, https://doi.org/10.1016/j.optmat.2014.10.061.

[44] V.K. Ravi, S. Saikia, S. Yadav, V.V. Nawale, A. Nag, $CsPbBr_3$/ZnS Core/shell type nanocrystals for enhancing luminescence lifetime and water stability, ACS Energy Lett. 5 (2020) 1794–1796, https://doi.org/10.1021/acsenergylett.0c00858.

[45] R. Sakai, H. Onishi, S. Ido, S. Furumi, Effective Mn-doping in $AgInS_2$/ZnS core/shell nanocrystals for dual photoluminescent peaks, Nanomaterials 9 (2019), https://doi.org/10.3390/nano9020263.

[46] B.F. Troque, S.A. Eliziário, M.J. Godinho, R.H.G.A. Kiminami, Síntese in situ pelo método hidrotérmico de heteroestruturas de titanato-ferritas e sua atividade fotocatalítica, Cerâmica 64 (2018) 248–253, https://doi.org/10.1590/0366-69132018643702265.

[47] Y. Yan, H. Yang, Z. Yi, R. Li, X. Wang, Enhanced photocatalytic performance and mechanism of Au@$CaTiO_3$ composites with Au nanoparticles assembled on $CaTiO_3$ nanocuboids, Micromachines 10 (2019) 1–16, https://doi.org/10.3390/mi10040254.

[48] U. Coleto Junior, R.A.C. Amoresi, C.A.M. Pereira, A.Z. Simões, M.A. Zaghete, E. S. Monteiro Filho, E. Longo, L.A. Perazolli, Influence of defects on photoluminescent and photocatalytic behavior of CaO/$SrTiO_3$ heterojunctions, Ceram. Int. 45 (2019) 15244–15251, https://doi.org/10.1016/j.ceramint.2019.05.013.

[49] M.N. Ha, F. Zhu, Z. Liu, L. Wang, L. Liu, G. Lu, Z. Zhao, Morphology-controlled synthesis of $SrTiO_3$/TiO_2 heterostructures and their photocatalytic performance for water splitting, RSC Adv. 6 (2016) 21111–21118, https://doi.org/10.1039/c6ra03472a.

[50] X. Xu, X. Wang, Perovskite nano-heterojunctions: synthesis, structures, properties, challenges, and prospects, Small Struct 1 (2020), 2000009, https://doi.org/10.1002/sstr.202000009.

[51] M.L. Moreira, E.C. Paris, G.S. do Nascimento, V.M. Longo, J.R. Sambrano, V. R. Mastelaro, M.I.B. Bernardi, J. Andrés, J.A. Varela, E. Longo, Structural and optical properties of $CaTiO_3$ perovskite-based materials obtained by microwave-assisted hydrothermal synthesis: an experimental and theoretical insight, Acta Mater. 57 (2009) 5174–5185, https://doi.org/10.1016/j.actamat.2009.07.019.

[52] C.H. Huang, Y.T. Yang, R.A. Doong, Microwave-assisted hydrothermal synthesis of mesoporous anatase TiO_2 via sol–gel process for dye-sensitized solar cells, Microporous Mesoporous Mater. 142 (2011) 473–480, https://doi.org/10.1016/j.micromeso.2010.12.038.

[53] C.L. Ücker, V. Goetzke, F.C. Riemke, M.L. Vitale, L.R.Q. de Andrade, M.D. Ücker, E.C. Moreira, M.L. Moreira, C.W. Raubach, S.S. Cava, Multi-photonic behavior of

Nb_2O_5 and its correlation with synthetic methods, J. Mater. Sci. 56 (2021) 7889–7905, https://doi.org/10.1007/s10853-021-05770-z.
[54] C.W. Raubach, L. Polastro, M.M. Ferrer, A. Perrin, C. Perrin, A.R. Albuquerque, P. G.C. Buzolin, J.R. Sambrano, Y.B.V. De Santana, J.A. Varela, E. Longo, Influence of solvent on the morphology and photocatalytic properties of ZnS decorated CeO_2 nanoparticles, J. Appl. Phys. 115 (2014), https://doi.org/10.1063/1.4880795.
[55] C.L. Ücker, L.T. Gularte, C.D. Fernandes, V. Goetzke, E. Ceretta, C.W. Raubach, M. L. Moreira, S.S. Cava, Investigation of the properties of niobium pentoxide for use in dye-sensitized solar cells, J. Am. Ceram. Soc. 102 (2019) 1884–1892, https://doi.org/10.1111/jace.16080.
[56] S. de C. Pereira, A.T. de Figueiredo, C.M. Barrado, M.H. Stoppa, T.O. dos Santos, F.M. Pontes, E. Longo, Fast and efficient microwave-assisted synthesis of $CaTiO_3$, Mater. Res. Express 4 (2017), 065014, https://doi.org/10.1088/2053-1591/aa7483.
[57] T.M. Mazzo, G.S. Do Nascimento Libanori, M.L. Moreira, W. Avansi, V. R. Mastelaro, J.A. Varela, E. Longo, Influence of titanium precursor on photoluminescent emission of micro-cube-shaped $CaTiO_3$, J. Lumin. 165 (2015) 130–137, https://doi.org/10.1016/j.jlumin.2015.03.028.
[58] L.H. Oliveira, J. Savioli, A.P. De Moura, I.C. Nogueira, M.S. Li, E. Longo, J. A. Varela, I.L.V. Rosa, Investigation of structural and optical properties of $CaTiO_3$ powders doped with Mg^{2+} and Eu^{3+} ions, J. Alloys Compd. 647 (2015) 265–275, https://doi.org/10.1016/j.jallcom.2015.05.226.
[59] I.M. Pinatti, T.M. Mazzo, R.F. Gonçalves, J.A. Varela, E. Longo, I.L.V. Rosa, $CaTiO_3$ and $Ca_{1-3x}Sm_xTiO_3$: photoluminescence and morphology as a result of hydrothermal microwave methodology, Ceram. Int. 42 (2016) 1352–1360, https://doi.org/10.1016/j.ceramint.2015.09.074.
[60] C.R. Strauss, D.W. Rooney, Accounting for clean, fast and high yielding reactions under microwave conditions, Green Chem. 12 (2010) 1340–1344, https://doi.org/10.1039/c0gc00024h.
[61] F.I. Pires, E. Joanni, R. Savu, M.A. Zaghete, E. Longo, J.A. Varela, Microwave-assisted hydrothermal synthesis of nanocrystalline SnO powders, Mater. Lett. 62 (2008) 239–242, https://doi.org/10.1016/j.matlet.2007.05.006.
[62] C.L. Ücker, V. Goetzke, S.R. Almeida, E.C. Moreira, M.M. Ferrer, P.L.G. Jardim, M.L. Moreira, C.W. Raubach, S. Cava, Photocatalytic degradation of rhodamine B using Nb_2O_5 synthesized with different niobium precursors: factorial design of experiments, Ceram. Int. 47 (2021), https://doi.org/10.1016/j.ceramint.2021.04.066, 20570–20578.
[63] H.E. Swanson, H.F. McMurdie, M.C. Morris, E.H. Evans, B. Paretzkin, J. H. Degroot, S.J. Carmel, Standard X-Ray Diffraction Powder Patterns Section 9 - Data for 63 Substances, 1971, https://doi.org/10.6028/NBS.MONO.25-9.
[64] R. Yi, G. Qiu, X. Liu, Rational synthetic strategy: from ZnO nanorods to ZnS nanotubes, J. Solid State Chem. 182 (2009) 2791–2795, https://doi.org/10.1016/j.jssc.2009.07.038.
[65] E.B. Manaia, R.C.K. Kaminski, B.L. Caetano, M. Magnani, F. Meneau, A. Rochet, C.V. Santilli, V. Briois, C. Bourgaux, L.A. Chiavacci, The critical role of thioacetamide concentration in the formation of ZnO/ZnS heterostructures by sol–gel process, Nanomaterials 8 (2018) 1–15, https://doi.org/10.3390/nano8020055.
[66] K.Y. Chen, Y.W. Chen, Preparation of barium titanate ultrafine particles from rutile titania by a hydrothermal conversion, Powder Technol. 141 (2004) 69–74, https://doi.org/10.1016/j.powtec.2004.03.002.
[67] T.M. Mazzo, M.L. Moreira, I.M. Pinatti, F.C. Picon, E.R. Leite, I.L.V. Rosa, J. A. Varela, L.A. Perazolli, E. Longo, $CaTiO_3$:Eu^{3+} obtained by microwave-assisted hydrothermal method: a photoluminescent approach, Opt. Mater. 32 (2010) 990–997, https://doi.org/10.1016/j.optmat.2010.01.039.
[68] R.F. Gonçalves, A.R.F. Lima, M.J. Godinho, A.P. Moura, J. Espinosa, E. Longo, A. P.A. Marques, Synthesis of Pr^{3+}-doped $CaTiO_3$ using polymeric precursor and microwave-assisted hydrothermal methods: a comparative study, Ceram. Int. 41 (2015) 12841–12848, https://doi.org/10.1016/j.ceramint.2015.06.121.
[69] E.M. Flores, C.W. Raubach, R. Gouvea, E. Longo, S. Cava, M.L. Moreira, Optical and structural investigation of ZnO@ZnS core–shell nanostructures, Mater. Chem. Phys. 173 (2016) 347–354, https://doi.org/10.1016/j.matchemphys.2016.02.022.
[70] K. Tesar, I. Gregora, P. Beresova, P. Vanek, P. Ondrejkovic, J. Hlinka, Raman scattering yields cubic crystal grain orientation, Sci. Rep. 9 (2019) 1–8, https://doi.org/10.1038/s41598-019-45782-z.
[71] Y. Wang, C.G. Niu, L. Wang, Y. Wang, X.G. Zhang, G.M. Zeng, Synthesis of fern-like Ag/AgCl/$CaTiO_3$ plasmonic photocatalysts and their enhanced visible-light photocatalytic properties, RSC Adv. 6 (2016) 47873–47882, https://doi.org/10.1039/c6ra06435c.
[72] T. Chen, Y. Zheng, Z. Lu, T. Xu, Y. Liu, X. Meng, G. Xu, G. Han, Hydrothermal synthesis and photocatalytic activity of the butterfly-like $CaTiO_3$ dendrites with dominant {101} facets, Nanotechnology 30 (2019), 475709, https://doi.org/10.1088/2058-8585/ab56b7.
[73] C. Peng, Z. Hou, C. Zhang, G. Li, H. Lian, Z. Cheng, J. Lin, Synthesis and luminescent properties of $CaTiO_3$: Pr^{3+} microfibers prepared by electrospinning method, Opt Express 18 (2010) 7543, https://doi.org/10.1364/oe.18.007543.
[74] M.E. Azim Araghi, N. Shaban, M. Bahar, Synthesis and characterization of nanocrystalline barium strontium titanate powder by a modified sol–gel processing, Mater. Sci. Pol. 34 (2016) 63–68, https://doi.org/10.1515/msp-2016-0020.
[75] C.C. Li, S.J. Chang, J.T. Lee, W.S. Liao, Efficient hydroxylation of $BaTiO_3$ nanoparticles by using hydrogen peroxide, Colloids Surfaces A Physicochem. Eng. Asp. 361 (2010) 143–149, https://doi.org/10.1016/j.colsurfa.2010.03.027.
[76] H. Yang, C. Han, X. Xue, Photocatalytic activity of Fe-doped $CaTiO_3$ under UV-visible light, J. Environ. Sci. (China) 26 (2014) 1489–1495, https://doi.org/10.1016/j.jes.2014.05.015.
[77] L.N. Liu, J.G. Dai, T.J. Zhao, S.Y. Guo, D.S. Hou, P. Zhang, J. Shang, S. Wang, S. Han, A novel Zn(II) dithiocarbamate/ZnS nanocomposite for highly efficient Cr^{6+} removal from aqueous solutions, RSC Adv. 7 (2017) 35075–35085, https://doi.org/10.1039/c7ra04259k.
[78] H. Qu, L. Cao, G. Su, W. Liu, R. Gao, C. Xia, J. Qin, Silica-coated ZnS quantum dots as fluorescent probes for the sensitive detection of Pb^{2+} ions, J. Nanoparticle Res. 16 (2014), https://doi.org/10.1007/s11051-014-2762-y.
[79] R.M. Krsmanović Whiffen, D.J. Jovanović, Z. Antić, B. Bártová, D. Milivojević, M. D. Dramićanin, M.G. Brik, Structural, optical and crystal field analyses of undoped and Mn^{2+}-doped ZnS nanoparticles synthesized via reverse micelle route, J. Lumin. 146 (2014) 133–140, https://doi.org/10.1016/j.jlumin.2013.09.032.
[80] S.K. Mani, S. Manickam, V. Muthusamy, R. Thangaraj, Antimicrobial activity and photocatalytic degradation properties of zinc sulfide nanoparticles synthesized by using plant extracts, J. Nanostructures. 8 (2018) 107–118, https://doi.org/10.22052/JNS.2018.02.001.
[81] T.M. Mok, S.K. O'Leary, The dependence of the Tauc and Cody optical gaps associated with hydrogenated amorphous silicon on the film thickness: αl Experimental limitations and the impact of curvature in the Tauc and Cody plots, J. Appl. Phys. 102 (2007), https://doi.org/10.1063/1.2817822.
[82] M.E. Sánchez-Vergara, J.C. Alonso-Huitron, A. Rodriguez-Gómez, J.N. Reider-Burstin, Determination of the optical gap in thin films of amorphous dilithium phthalocyanine using the Tauc and Cody models, Molecules 17 (2012) 10000–10013, https://doi.org/10.3390/molecules170910000.
[83] J. Tauc, Absorption edge and internal electric fields in amorphous semiconductors, Mater. Res. Bull. 5 (1970) 721–729, https://doi.org/10.1016/0025-5408(70)90112-1.
[84] K. Ueda, H. Yanagi, H. Hosono, H. Kawazoe, Study on electronic structure of $CaTiO_3$ by spectroscopic measurements and energy band calculations, J. Phys. Condens. Matter 11 (1999) 3535–3545, https://doi.org/10.1088/0953-8984/11/17/311.
[85] P. Guo, J. Jiang, S. Shen, L. Guo, ZnS/ZnO heterojunction as photoelectrode: type II band alignment towards enhanced photoelectrochemical performance, Int. J. Hydrogen Energy 38 (2013) 13097–13103, https://doi.org/10.1016/j.ijhydene.2013.01.184.
[86] C.W. Raubach, M.Z. Krolow, M.F. Mesko, S. Cava, M.L. Moreira, E. Longo, N.L. V. Carreño, Interfacial photoluminescence emission properties of core/shell Al_2O_3/ZrO_2, CrystEngComm 14 (2012) 393–396, https://doi.org/10.1039/c1ce06099f.
[87] C.W. Raubach, A.F. Gouveia, Y.V.B. De Santana, J.A. Varela, M.M. Ferrer, M.S. Li, E. Longo, Towards controlled synthesis and better understanding of blue shift of the CaS crystals, J. Mater. Chem. C 2 (2014) 2743–2750, https://doi.org/10.1039/c3tc32115k.
[88] F.V. Motta, A.P.A. Marques, J.W.M. Espinosa, P.S. Pizani, E. Longo, J.A. Varela, Room temperature photoluminescence of BCT prepared by complex polymerization method, Curr. Appl. Phys. 10 (2010) 16–20, https://doi.org/10.1016/j.cap.2009.04.005.
[89] C.W. Raubach, L. Polastro, M.M. Ferrer, A. Perrin, C. Perrin, A.R. Alburquerque, P.G.C. Buzolin, J.R. Sambrano, Y.V.B. De Santana, J.A. Varela, E. Longo, Influence of solvent on the morphology and photocatalytic properties of ZnS decorated CeO_2 nanoparticles, J. Appl. Phys. 115 (2014), https://doi.org/10.1063/1.4880795.
[90] A. Franco, M.C. Neves, M.M.L.R. Carrott, M.H. Mendonça, M.I. Pereira, O. C. Monteiro, Photocatalytic decolorization of methylene blue in the presence of TiO_2/ZnS nanocomposites, J. Hazard Mater. 161 (2009) 545–550, https://doi.org/10.1016/j.jhazmat.2008.03.133.
[91] D. Chen, F. Huang, G. Ren, D. Li, M. Zheng, Y. Wang, Z. Lin, ZnS nano-architectures: photocatalysis, deactivation and regeneration, Nanoscale 2 (2010) 2062–2064, https://doi.org/10.1039/c0nr00171f.
[92] Y. Yan, H. Yang, X. Zhao, R. Li, X. Wang, Enhanced photocatalytic activity of surface disorder-engineered $CaTiO_3$, Mater. Res. Bull. 105 (2018) 286–290, https://doi.org/10.1016/j.materresbull.2018.05.008.
[93] A. Kumar, C. Schuerings, S. Kumar, A. Kumar, V. Krishnan, Perovskite-structured $CaTiO_3$ coupled with g-C_3N_4 as a heterojunction photocatalyst for organic pollutant degradation, Beilstein J. Nanotechnol. 9 (2018) 671–685, https://doi.org/10.3762/bjnano.9.62.
[94] S. Guan, R. Li, X. Sun, T. Xian, H. Yang, Construction of novel ternary Au/$LaFeO_3$/Cu_2O composite photocatalysts for RhB degradation via photo-Fenton catalysis, Mater. Technol. (2020) 1–13, https://doi.org/10.1080/10667857.2020.1782062, 00.
[95] R.G. Pearson, Absolute electronegativity and hardness: application to inorganic chemistry, Inorg. Chem. (1997) 734–740.
[96] H. Yang, A short review on heterojunction photocatalysts: carrier transfer behavior and photocatalytic mechanisms, Mater. Res. Bull. 142 (2021), 111406, https://doi.org/10.1016/j.materresbull.2021.111406.
[97] G.J. Lee, J.J. Wu, Recent developments in ZnS photocatalysts from synthesis to photocatalytic applications — a review, Powder Technol. 318 (2017) 8–22, https://doi.org/10.1016/j.powtec.2017.05.022.
[98] D. Lin, H. Wu, R. Zhang, W. Zhang, W. Pan, Facile synthesis of heterostructured ZnO-ZnS nanocables and enhanced photocatalytic activity, J. Am. Ceram. Soc. 93 (2010) 3384–3389, https://doi.org/10.1111/j.1551-2916.2010.03855.x.

[99] C.W. Raubach, Y.V.B. De Santana, M.M. Ferrer, P.G.C. Buzolin, J.R. Sambrano, E. Longo, Photocatalytic activity of semiconductor sulfide heterostructures, Dalton Trans. 42 (2013) 11111–11116, https://doi.org/10.1039/c3dt50374g.
[100] A. Kudo, Y. Miseki, Heterogeneous photocatalyst materials for water splitting, Chem. Soc. Rev. 38 (2009) 253–278, https://doi.org/10.1039/b800489g.
[101] T. Cheng, H. Gao, R. Li, S. Wang, Z. Yi, H. Yang, Flexoelectricity-induced enhancement in carrier separation and photocatalytic activity of a photocatalyst, Appl. Surf. Sci. 566 (2021), 150669, https://doi.org/10.1016/j.apsusc.2021.150669.